PHYSICAL REVIEW B **71**, 054108 (2005)

Structural phase transition of Fe grown on Au(111)

D. T. Dekadjevi and B. J. Hickey
Department of Physics and Astronomy, E. C. Stoner Laboratory, University of Leeds, Leeds LS2 9JT, United Kingdom

S. Brown
ESRF, BP 220, F39043 Grenoble, France

T. P. A. Hase, B. D. Fulthorpe, and B. K. Tanner
Department of Physics, University of Durham, Durham DH1 3LE, United Kingdom

(Received 5 November 2004; published 18 February 2005)

Detailed structural studies of the growth of Fe on Au(111) have resolved the long-standing controversy about the nature of the structural phase change in the Fe/Au system. It has been thought that the first few layers of Fe on Au in this orientation grew as fcc. Here we show that the first few layers of Fe grow epitaxially on Au to form a rotated, strained face-centered structure. Subsequently the entire Fe layer relaxes via two distinct lattice distortions into bcc Fe.

DOI: 10.1103/PhysRevB.71.054108 PACS number(s): 81.15.−z, 68.55.−a, 75.70.Cn, 73.63.−b

I. INTRODUCTION

It is well known that the magnetic properties of ultrathin films depend upon the crystalline phase of the material. In epitaxial growth, this phase can be different for the first few monolayers (ML) compared with subsequent layers. This is related to the growth conditions which influence the diffusion length of the atoms as well as the lattice parameter and surface free energy of the underlayer. These effects can result in a thickness dependence of the structure and consequently of the magnetic properties.

Recently there has been a huge interest in using epitaxy to study interesting phases of elements such as Fe. For example, γFe, which is fcc, is predicted to be antiferromagnetic under a 1% tensile stain but normally only exists above temperatures of 1184 K. Various substrates have been used to seed the fcc growth of Fe such as Cu(001),[1,2] Co(001), or Ni(001),[3] and these systems have been extensively studied. It was shown that a phase transition from fcc to bcc occurs via an fct phase with accompanying complicated magnetic behavior. The similarity between these three systems has been attributed to the nearly identical in-plane structure of the underlayers. These studies confirmed theoretical predictions that the magnetic properties of Fe is a function of its lattice parameter.[4,5]

Electron channeling effects have been demonstrated in the transport properties of Fe/Au(100) and Fe/Au(111).[6,33] Crucial to our investigations has been an understanding of the structural differences between the two crystallographic orientations. Early structural studies using scanning tunneling microscopy[7] suggested that for thicknesses less than 1 nm, the Fe layer had grown pseudomorphically to the fcc Au(111). This idea was contradicted by studies[8,9] of the magnetic properties where the conclusion was that only bcc Fe was present at any thickness. However, no confirmation by structural analysis was given by these authors. Other structural studies of Fe samples with a thickness greater than 1 nm have shown that the Fe is bcc(110) oriented with a Nishiyama-Wasserman[10,11] (NW) or Kurdjumov-Sachs[12] (KS) epitaxial relationship depending on the growth temperature. These different structural studies are restricted either to in-plane structure and/or thicknesses either below or above the phase transition. More recently medium-energy ion scattering[13] showed that a relaxation occurs but no details concerning the relaxed structure or epitaxial relationship with the underlayer were determined.

In this paper, we present a structural study of the evolution of the crystallography of Fe layers deposited on Au(111). We study in detail the growth of Fe from 1 ML up to a thickness where the Fe is relaxed. In the first part, the crystallography along the normal to the surface is probed using high-angle x-ray diffraction (HAXRD). In the second part, we concentrate on the in-plane structure using reflection high-energy electron diffraction (RHEED) as an *in situ* probe and grazing-incidence surface x-ray diffraction (GIXD) as an *ex situ* technique to probe in-plane structure after the deposition of overlayers.

II. EXPERIMENTAL PROCEDURE

The samples were grown in a VG-80 Semicon molecular beam epitaxy (MBE) system with a base pressure of 5×10^{-11} mbar. It is equipped with a RHEED electron gun working at 12 kV and the RHEED patterns were captured with a charge-coupled-device camera and a frame grabber card used in connection with a personal computer. The data were analyzed using the software KSA300 described elsewhere.[14] The angle of incidence of the electron beam was below 0.6° which limited the electron mean free path to the first 2 ML.[15] High-quality $Al_2O_3(11\overline{2}0)$ crystals were used as substrates. They were rinsed in acetone and isopropanol and then annealed at 950 °C for 1 h. Because it is well known that the deposition of a Nb layer on this substrate is an excellent buffer for epitaxial growth of metallic multilayers,[16–18] a 130-ML Nb buffer layer was evaporated by an *e*-gun at a rate of 25 ML/min and at a substrate temperature of 950 °C. A first Au layer 130 ML thick was deposited using a Knudsen cell at a rate of 5 ML/min and at a substrate temperature of 250 °C. A single Fe layer and the superlattice of Fe and Au layers were deposited at 30 °C and at a rate of 5 ML/min.

To study the evolution of the Fe crystalline structure as a function of its thickness, a 20-ML single Fe layer was grown on the Au buffer. The growth was interrupted at each ML to perform an *in situ* RHEED analysis at the surface of the sample. An *ex situ* x-ray analysis was carried out on several superlattices for information concerning the crystallinity along the normal of the surface. These were grown during the same run with nominal structures Nb 130 ML/Au 130 ML/{Fe X ML/Au 9 ML/}×20 where $X=3,6,9$. The GIXD measurements were performed at the XMaS Beamline, ESRF Grenoble.[19] Through the use of focusing optics it is possible to achieve an incident beam intensity of the order of 10^{12} cps. The beamline is equiped with an 11-axis Huber diffractometer, allowing scans to be performed in both the vertical and horizontal plane of the film. A Bicron scintillation detector was used in conjunction with Soller slits of 0.1° angular acceptance. In the grazing-incidence scattering geometry an incident beam angle is selected by tilting the entire diffractometer assembly with respect to the beam. This method ensures that, although the diffractometer axes are now offset to the beam, all axes still scan in the same horizontal plane. An incident beam angle of $\theta=0.2°$, below the critical angle for total external reflection, was used, limiting the $1/e$ depth of the intensity of the evanescent wave, at $\lambda=1.033$ Å, to approximately 40 Å. In GIXD, diffraction planes perpendicular to the surface are chosen and two types of scan performed. Rocking curves in which the sample only was rotated about its surface normal (ϕ scans) measured the in-plane mosaic and coherence length. Coupled ϕ-2θ scans of specimen and detector in a 1:2 ratio measured the in-plane lattice parameter. The in-plane Bragg peak widths may be broadened by inhomogeneous in-plane strain. A full in-plane reciprocal space map can be obtained by combining a sequence of ϕ-2θ scans at different ϕ values.

Grazing-incidence specular and diffuse reflectivity measurements were used to measure layer thickness and interface structure. As the scattering vector is small in comparison to the value of a reciprocal lattice vector, these latter measurements are sensitive only to electron density. (For these measurements the ϕ angle remains constant.)

III. OUT-OF-PLANE STRUCTURE

High-angle, coupled θ-2θ diffraction scans running longitudinally down the reciprocal lattice vector are shown in Fig 1. There is a well-defined zero-order multilayer peak with several satellite diffraction orders, equally spaced about the zero-order peak. The scattering is dominated by the Au layers and is largely insensitive to imperfections within the Fe layers. The peak positions are within 0.3% agreement of those calculated from the bulk lattice parameters, weighted by relative layer thickness. This confirms the Au in the multilayers to be (111) oriented with no other orientations present and minimal out-of-plane strain. The sharp, well-defined peaks, visible out to high order, indicate the interfaces to be crystallographically abrupt with well-defined, epitaxial layers and little interdiffusion.

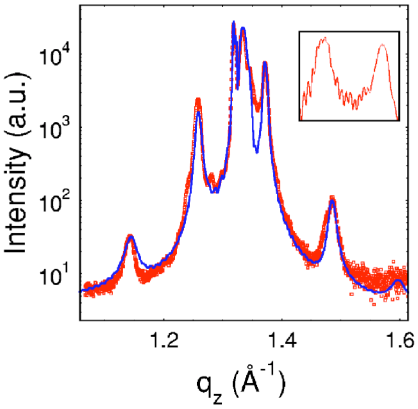

FIG. 1. (Color online) HAXRD scan of an FeAu(111) multilayer with 3 ML of Fe taken at a wavelength of 1 Å. The solid line is a fit using the simulation program SUPREX. The inset shows the detail of the fringes between satellite peaks on a 9-ML sample. These data confirm the high quality of the superlattice.

Since the phase transition or structural disorder can contribute to the full width half maximum (FWHM) of the main Bragg peak, simulations were carried out using a modified version of the SUPREX code.[20] With the original code, it is either possible to simulate a bilayer structure or a multilayer. For the particular samples studied here, where a multilayer was deposited on two buffers, a modification was required to take into account the scattering of all the layers. The Nb and Au buffers were modeled as the bilayer structure and the calculated intensity was added to the simulation obtained from the pure multilayer. This incoherent approximation is equivalent to

$$|S(q)|^2 + |B(q)|^2 \approx |S(q) + B(q)|^2, \tag{1}$$

where $S(q)$ is the scattering amplitude from the N bilayers and $B(q)$ the one from both of the buffers. The multilayer satellite peaks and the Bragg peaks arising from the buffers are sufficiently separated to allow us to use the incoherent approximation. The fit in Fig. 1 is satisfactory, bearing in mind that diffuse scatter is not included in the model.

In these simulations, two of the parameters in SUPREX have an influence on the width of the main Bragg peaks: the "continuous roughness" defined as the continuous atomic level disorder at each interface and the "discrete roughness" defined as a Gaussian variation of the number of planes. Continuous fluctuations of the interface thickness can explain the loss of long-range order and the discrete roughness in the material of one layer will broaden the peaks at the position of another material.[21,22] The influence of the other parameters of the fitted profile was restricted to the satellite peaks. Parameters used to fit the curve in Fig. 1 are listed in Table I.

Broadening of the main Bragg peak for samples with more than 5 ML of Fe could not be simulated. This broadening is attributed to a reduction of the bilayer coherence length brought about by the presence of a different Fe phase.

TABLE I. Suprex parameters used in fitting the 3-ML Fe data in Fig. 1. d is the interplanar spacing, N_{mono} is the number of monolayers, c is the continuous roughness, I is the interdiffusion, and α_i is the decay length of the interdiffusion. The fit was found without any stress and negligible monolayer fluctuations.

	d (Å)	N_{mono}	c (Å)	I (%)	α_i
Fe	2.120±0.005	3.21±0.01	0.06±0.01	10±2	5±2
Au	2.355±0.005	8.85±0.03	—	10±2	5±2

Indeed, the in-plane residual stress will vary because the plastic deformation of the metal depends on the type of crystallites (NW bcc or fcc in-plane structure). This results in a nonuniform strain, normal to the plane, which causes a broadening of the peaks.[23] In agreement with this the out-of-plane coherence length determined from the FWHM using the Scherrer formula is reduced with increasing thickness of Fe layers.

We note from the inset of Fig. 1 the well-defined thickness fringes modulating the main Bragg peak, particularly evident on thicker samples such as the 9-ML example shown. Indeed, these are not arising solely from the top and bottom of the N bilayers since $(N-2)$ fringes are expected between the peaks. They are therefore due to the scattering from the whole of the sample including the Nb and Au buffers. Their periodicity corresponds to a thickness of 580 Å, in agreement with the nominal thickness of 600 Å.

The average interplanar spacing (d_x) was determined from the zero-order peak whereas the bilayer spacing (Λ_x) was determined from the position of the satellite peaks using[24]

$$\frac{2\sin\theta}{\lambda} = \frac{1}{d_x} \pm \frac{n}{\Lambda_x}. \tag{2}$$

From the definition of d_x and Λ_x, it easy to show that the Fe interplanar spacing d_{Fe} is given by

$$d_{\mathrm{Fe}} = \frac{\Lambda_x - N_{\mathrm{Au}} d_{\mathrm{Au}}}{\Lambda_x - N_{\mathrm{Au}} d_x} d_x. \tag{3}$$

All the parameters of this equation are determined experimentally except the Au interplanar spacing which is assumed to be equivalent to the bulk since the RHEED and GIXD show that the in-plane structure of the Au overlayers are bulk like in these samples. At any thickness, the out-of-plane lattice parameter of the Fe layer is much shorter than the fcc Au(111) and approximates the bulk Fe bcc(110) for large Fe thickness.

Simulation of x-ray specular and diffuse reflectivity measurements enabled an independent measurement of the superlattice periodicity as well as the interface roughness. The off-specular scans exhibited the same periodic features as the specular scans indicating that a high proportion of the interface roughness is correlated in nature. Figure 2(a) shows a specular scan of the reflectivity of a 9-ML Fe sample. The excellent agreement between simulated and experimental data allows an accurate determination of the layer thickness and interface width to be obtained. $\Lambda_{low,x}$, the bilayer spacing determined from low-angle reflectivity scans, is in remarkably good agreement with that determined from the high-angle scans. The bilayer, buffer, and seed layer thicknesses were all found to be close to the nominal thickness.

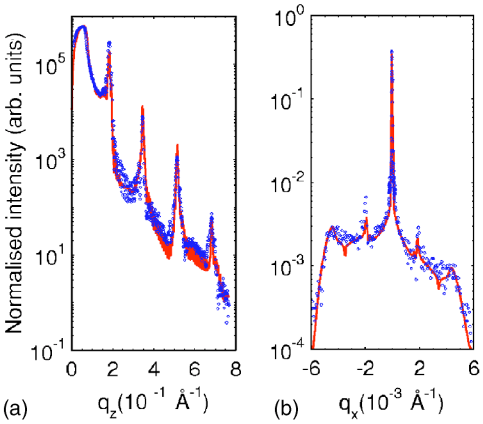

FIG. 2. (Color online) Reflectivity scan of an FeAu(111) multilayer with 9 ML of Fe. The left frame shows the specular scatter with four orders of Bragg reflections and Kiessig fringes clearly visible. The frame on the right is a measurement of the diffuse scatter where the specular ridge is clearly visible as are hints of the Yoneda wings. The solid lines represent fits to the data.

The nature of the interface roughness and lateral interface morphology was determined by fitting simulated data from model structures to transverse diffuse data [Fig. 2(b)]. For each sample, transverse diffuse data at several scattering vectors were modeled simultaneously. While time consuming, such a method is essential in locating the true global minimum for the match. The interfaces possess a roughness which is predominantly correlated in nature with a correlated to uncorrelated ratio of 15:1, and there was no observable compositional grading. For the 4-ML-thick Fe multilayer, the rms roughness was measured to be 3.3±0.3 Å and the in-plane correlation length was 250±10 Å. For an Fe thickness of 7 ML, a slightly lower rms value of 2.5±0.3 Å was found with a correlation length of 195±10 Å.

Table II shows the parameters determined from the high-angle x-ray and specular reflectivity data.

IV. IN-PLANE STRUCTURE

In Fig. 3 we show a model of the various row spacings which are present in the (110) plane of Fe. The growth mode of one metal on another is determined by surface energy considerations and the degree of lattice mismatch. In the case of Fe on Au, islands form because there is both a surface energy difference and a lattice mismatch. There are two possible crystalline orientations which correspond to different growth modes of nucleated islands. The preferred directions are those in which the most densely packed rows $(\langle 0\bar{1}1\rangle)$ in the fcc(111) plane are parallel to one of the densely packed rows in the bcc(110) plane $(\langle \bar{1}11\rangle, \langle 1\bar{1}1\rangle, \langle 001\rangle)$. The first two are the KS orientations and the last is the NW orientation. From these possibilities, the preferred one will depend on whether the distance between the corresponding rows is the same in the two crystals. In our samples, the ratio of

TABLE II. Measured lattice parameter (d_x) and deduced Fe lattice parameter (d_{Fe}) determined from fitting the HAXRD data using SUPREX. Λ_x and $\Lambda_{low,x}$ are the bilayer periods deduced from HAXRD and reflectivity measurements, respectively.

	d_x	Λ_x (Å)	$\Lambda_{low,x}$ (Å)	d_{Fe} (Å)
3 ML Fe	2.286 ± 0.005	27.61 ± 0.07	27.9 ± 0.5	2.12 ± 0.07
6 ML Fe	2.248 ± 0.005	34.37 ± 0.08	34.0 ± 0.5	2.11 ± 0.06
9 ML Fe	2.200 ± 0.005	40.66 ± 0.08	39.9 ± 0.5	2.07 ± 0.06

nearest-neighbor distances in the bulk metals, $r = a_{\mathrm{Au}}/a_{\mathrm{Fe}} = 1.16 \pm 0.06$, is close to the value of $r = 1.155$ for which the NW orientation is preferred, based on calculations of the energy contributions of misfit dislocations and strain. The value of r for the KS orientation is 1.08. However, in the presence of defects or nonuniform strain, the theory suggests that pseudomorphic and KS growth modes can occur.[25–27]

A. Fe thinner than 5 ML

Analysis of the RHEED patterns reveals both changes in the topography of the surface and changes in the crystallographic structure of the surface.[28,29] The FWHM of the specular streaks was recorded with the beam along the $\langle 0\bar{1}1\rangle$ and $\langle \bar{2}11\rangle$ directions in the Au. The FWHM has been deconvoluted from the instrumental broadening and the average in-plane coherence length determined. The instrumental broadening corresponds to a coherence length of the electron beam estimated at 1800 ± 100 Å from the finite convergence and finite energy spread of the electron beam.[30] The lattice spacing calibration was carried out on the well-oriented surface of the Nb(110)buffer.

The RHEED pattern along $\langle 0\bar{1}1\rangle$ and $\langle \bar{2}11\rangle$ azimuths of the Au buffer exhibited fine and continuous streaks as shown in Fig. 4. The FWHM of these streaks indicate an average in-plane coherence length of 1300 ± 150 Å.

Figure 4 also shows the two main features observed from the RHEED patterns at the surface of the Fe layers. The first feature consists of discontinuous streaks at an early stage of the deposition. This suggests a nucleation of Fe islands on the Au surface which is expected because of the much higher surface free energy of Fe ($2.9\ \mathrm{J/m^2}$) compared to Au ($1.6\ \mathrm{J/m^2}$). Previous experimental studies,[7] where the growth conditions of Fe on Au(111) substrate were similar, showed the coalescence of early formed Fe islands leading to layers which are atomically flat with terraces of order 100 Å. The important point is the coincidence of the RHEED pattern for the 4 ML Fe layer with that of the Au.

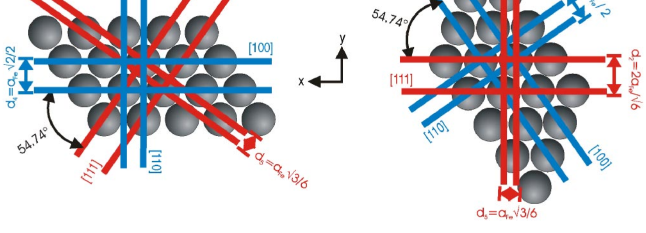

FIG. 3. (Color online) The (110) plane of Fe showing the various lattice spacings and the two epitaxial growth modes: NW and KS.

Before the critical thickness of 5 ML, where the splitting of the streaks occurs, the ratio between the lattice spacing along $\langle \bar{2}11\rangle$ Au and that along $\langle 0\bar{1}1\rangle$ is equal to $\sqrt{3}$. Also, these lattice spacings were repeatedly found with a 60° rotation of the sample. This is characteristic of (111) plane sixfold symmetry. The Fe layer is therefore growing epitaxially to the Au adopting an fcc(111) surface. The central images in Fig. 4 are saturated in order to show the weaker features. Line scans across images with shorter exposures enable the lattice parameter to be determined with an uncertainty of 0.5%. We find the in-plane lattice parameter of the strained Fe to be 4.00 ± 0.02 Å.

The second feature only appears for Fe which is thicker than 5 ML. A progressive splitting of the streaks located on each side of the specular streak is observed along the $\langle 0\bar{1}1\rangle$ and $\langle \bar{2}11\rangle$ crystallographic directions of the Au. This could arise from diffraction on a vicinal surface;[31] however, in this case the specular streak would also be split, which is not observed, showing that the Fe is growing in two different epitaxial structures.[32]

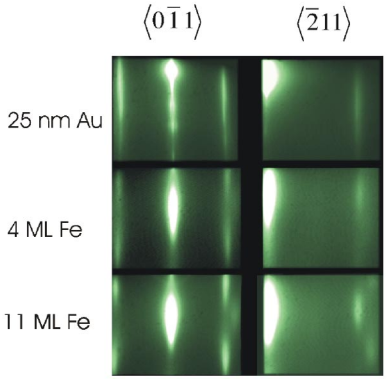

FIG. 4. (Color online) RHEED images of the growth of Au on sapphire and Fe on Au. The two columns indicate the direction of the electron beam in the (111) plane, and the row labels indicate the surface under study. The second row shows the growth of a thin Fe layer where the coincidence of the Fe and Au streaks indicate that the Fe has grown with the same lattice constant as the Au. The third row shows the pattern for much thicker Fe. Note the development of two lattice constants evident from the additional streaking in the righthand frame.

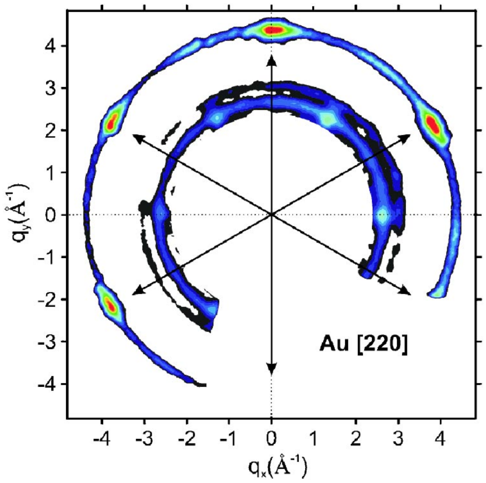

FIG. 5. (Color online) GIXD data for a multilayer of 4-ML-thick Fe layers on Au. The large peaks are along the Au ⟨110⟩ directions—note the small shoulders which are due to the strained, rotated Fe. The angle of rotation from the the Au ⟨110⟩ direction is 24°. At lower wave vector there is evidence of the NW orientation beginning to form.

For the deposition of the first 3 ML of Au on Fe, the RHEED pattern also exhibits discontinuous streaks and their position shows a 2% strain of the $\langle 0\bar{1}1\rangle$ interatomic rows and 1% strain along $\langle\bar{2}11\rangle$, compared to bulk. However, a definitive conclusion cannot be reached because this could be either a real strain or a result of the finite electron penetration depth. For greater thicknesses, the streaks are continuous, and the distance between them remains stable with the growth of further layers. This indicates that the Au has a well-ordered 2D surface[28] and that the stress is relaxed before the deposition of the fourth ML. The lattice parameter of the (111) fcc plane is then found to be 4.06±0.02 Å which agrees with the bulk value of 4.08 Å.

Figure 5 shows the in-plane GIXD data from which a reciprocal space map is constructed.

Near a detector angle of 43°, corresponding to a scattering vector $q=4.36$ Å^{-1}, are the Au peaks corresponding to the (220) reflections. Between the Au (220) peaks, there are shoulders to the scatter in a radial direction in reciprocal space. Such shoulders indicate a distribution of orientations at constant lattice parameter, showing that Fe is growing epitaxially on the Au but with the lattice rotated by 24°. A second feature of the reciprocal space map is the emerging peaks at about $q=2.58$ Å^{-1} which is the NW orientation of the nucleating island growth. The lattice parameters determined from RHEED and GIXD analysis are summarized in Table III.

B. Fe thicker than 5 ML

Well-defined sixfold symmetry in the GIXD data shows the Au layers to be deposited with good (111) epitaxy in the plane of the film (Fig. 6). Variations in the peak and background intensity are due to the sample plane not being exactly perpendicular to the ϕ axis of rotation as well as the sample shape. The Au peaks are broadened due to the presence of underlying peaks from the Fe layers. The shoulders present in the thinner Fe multilayers have now disappeared.

TABLE III. Interatomic row spacings from RHEED and GIXD.

	RHEED	GIXD
Under 5 ML	4.06±0.02	4.06±0.01
Over 5 ML NW $\langle\bar{2}11\rangle$	2.06±0.02	2.036±0.005
Over 5 ML KS $\langle\bar{2}11\rangle$	2.36±0.02	2.363±0.005

As the thickness of the Fe increases, the interface strain is relaxed and two orientations for the Fe appear. Near scattering vectors of $q=2.55$ Å^{-1} and $q=2.97$ Å^{-1} there are peaks corresponding to two structures with different lattice constants. These correspond to the KS and NW epitaxial structures. The absence of the shoulders on the Au 220 peaks signifies that with the increasing number of overlayers of Fe, the strain at the Au interface has been overcome, causing the *entire* Fe layer to reorder into a bcc structure. The GIXD data therefore confirm that a structural transformation has occurred.

Since RHEED analysis gives information on the spacing between equivalent rows of atoms parallel to the incident beam, the presence of the NW orientation is indicated by a spacing of $a_{\mathrm{Fe}}/2=1.435$ Å along the $\langle\bar{2}11\rangle$ fcc and $a_{\mathrm{Fe}}/\sqrt{2}=2.029$ Å along the $\langle 0\bar{1}1\rangle$ fcc.[32] On the other hand, the presence of the KS orientation would be indicated by a lattice spacing of $(2a_{\mathrm{Fe}}/\sqrt{6})=2.348$ Å along the $\langle 0\bar{1}1\rangle$ fcc and $(a_{\mathrm{Fe}}\sqrt{3}/6)=0.828$ Å along the $\langle\bar{2}11\rangle$ fcc, the spacing between $\langle\bar{2}11\rangle$ bulk Fe. In Fig. 7 is shown the evolution of the lattice parameters as a function of Fe thickness. The NW

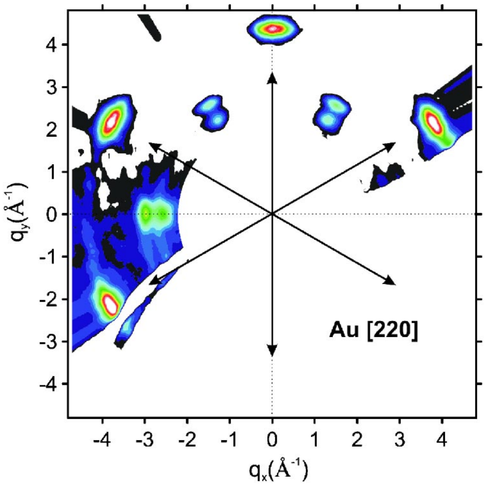

FIG. 6. (Color online) GIXD data for 10-ML Fe layers on Au. The large peaks are along the Au ⟨110⟩ directions—note the small shoulders which were present in the thinner Fe have now vanished. At 30° to the Au ⟨110⟩ directions are peaks at scattering vector of $q=2.55$ Å^{-1} and $q=2.97$ Å^{-1} representing the KS and NW growth modes of Fe.

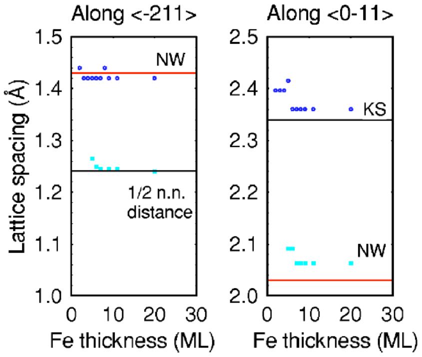

FIG. 7. (Color online) Evolution of the interatomic row spacings with the Fe thickness. The expected parameters for the NW and KS orientations are shown as horizontal lines.

orientation is clearly visible but only one characteristic of the KS orientation is present. Along $\langle\bar{2}11\rangle$ the spacing was found to be 1.24 Å, half the $\langle\bar{1}11\rangle$ bulk interatomic spacing. This indicates that the atomic row perpendicular to the [111] direction is cutting the [111] bulk lattice planes in half. From these observations, the conclusion is that, beyond 5 ML, the surface consists of two different centered rectangular nets, one corresponding to a relaxed NW bcc(110) Fe plane and the other a nearly relaxed KS bcc(110) Fe.

The evolution of the average in-plane coherence length measured by RHEED, shown in Fig 8, provides confirmation of this growth mode. The increase of the in-plane coherence length to 70±5 Å after the deposition of 5 ML is consistent with the coalescence of islands. A larger in-plane correlation length determined by diffuse x-ray reflectivity measurements is consistent with the values obtained by RHEED. However, the RHEED coherence length measures the size of the crystalline diffracting unit whereas the x-ray reflectivity is insensitive to short-range order.

V. CONCLUSIONS

The combination of in-plane and out-of-plane analyses achieved through RHEED and x-ray scattering provides incontrovertible evidence for a structural phase transition at an Fe thickness near 5 ML, 10 Å. For Fe layers thinner than 5 ML, the in-plane structure is a rotated epitaxial structure with respect to Au(111). The rotation provides a mechanism for accommodating the interface strain[34] and the out-of-plane lattice constant is consistent with an fcc structure.[7] There is no evidence for pseudomorphic growth. For layers thicker than 5 ML the structure relaxes to bulklike (110)-oriented bcc. The relaxation mechanism is mediated by the nucleation of two different modifications of the bcc structure, the Nishiyama-Wasserman and Kurdjumov-Sachs forms. These are rotated with respect to each other within the plane. For thick Fe layers the out-of-plane lattice constant approaches that of the bulk. The in-plane coherence length rises with thickness up to 5 ML after which it saturates. The out-of plane coherence length decreases monotonically over the whole thickness range investigated. The growth of Au on Fe does not influence the underlying Fe structure at all. However, we have shown that beyond 5 ML in thickness, the entire Fe layer transforms from strained fcc to bcc Fe.

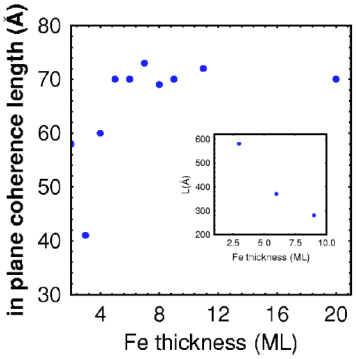

FIG. 8. (Color online) Evolution of the average in-plane coherence length with Fe thickness. The value saturates after the phase transition at an Fe thickness of about 5 ML. The inset shows the out-of-plane coherence length determined from HAXRD and using the Debye-Scherrer formula.

ACKNOWLEDGMENTS

This work was supported by EPSRC. The XMAS beamline staff at the ESRF are thanked for outstanding technical support. Thanks are expressed to Professor Ivan Schuller for making SUPREX available to us.

---

[1] J. Shen, C. V. Mohan, P. Ohresser, M. Klaua, and J. Kirschner, Phys. Rev. B **57**, 13 674 (1998).

[2] J. Giergiel, J. Shen, J. Woltersdorf, A. Kirilyuk, and J. Kirschner, Phys. Rev. B **52**, 8528 (1995).

[3] W. L. O'Brien and B. P. Tonner, Phys. Rev. B **52**, 15 332 (1995).

[4] V. L. Moruzzi, P. M. Marcus, and J. Kubler, Phys. Rev. B **39**, 6957 (1989).

[5] C. S. Wang, B. M. Klein, and H. Krakauer, Phys. Rev. Lett. **54**, 1852 (1985).

[6] D. Dekadjevi *et al.*, Phys. Rev. Lett. **86**, 5787 (2001).

[7] J. A. Stroscio, D. T. Pierce, R. A. Dragoset, and P. N. First, J. Vac. Sci. Technol. A **10**, 1981 (1992).

[8] G. Lugert, W. Robl, L. Pfau, M. Brockmann, and G. Bayreuther, J. Magn. Magn. Mater. **121**, 498 (1993).

[9] G. Bayreuther, in *Magnetism and Structure in Systems of Reduced Dimension*, edited by R. F. C. Farrow *et al.* (Plenum Press, New York, 1993), p. 467.

[10] G. Wasserman, Arch. Eisenhuettenwes. **16**, 647 (1933).

[11] Z. Nishiyama, Sci. Rep. Tohoku Univ., Ser. 1 **23**, 638 (1934).

[12] G. Kurdjumov and G. Sachs, Z. Phys. **64**, 325 (1930).

[13] T. C. Q. Noakes, P. Bailey, P. K. Hucknall, K. Donovan, and M. A. Howson, Phys. Rev. B **58**, 4934 (1998).

[14] D. Barlett *et al.*, Rev. Sci. Instrum. **62**, 1263 (1991).

[15] M. P. Seah and W. A. Dench, Surf. Interface Anal. **1**, 2 (1978).

[16] O. Fruchart, S. Jaren, and J. Rothman, Appl. Surf. Sci. **135**, 218 (1998).

[17] P. M. Reimer, H. Zabel, C. P. Flynn, and J. A. Dura, Phys. Rev. B **45**, 11 426 (1992).

[18] A. Gibaud, R. A. Cowley, D. F. McMorrow, R. C. C. Ward, and M. R. Wells, Phys. Rev. B **48**, 14 463 (1993).

[19] S. B. Brown *et al.*, J. Synchrotron Radiat. **8**, 1172 (2001).

[20] I. K. Schuller, Phys. Rev. Lett. **44**, 1597 (1980); W. Sevenhans *et al.*, Phys. Rev. B **34**, 5955 (1986); E. E. Fullerton *et al.*, *ibid.* **45**, 9292 (1992); D. M. Kelly, E. E. Fullerton, J. Santamaria, and I. K. Schuller, Scr. Metall. Mater. **33**, 1603 (1995).

[21] W. Sevenhans, M. Gijs, Y. Bruynseraede, H. Homma, and I. K. Schuller, Phys. Rev. B **34**, 5955 (1986).

[22] J. P. Locquet, D. Neerinck, L. Stockman, Y. Bruynseraede, and I. K. Schuller, Phys. Rev. B **39**, 13 338 (1989).

[23] B. D. Cullity, *Elements of X-ray Diffraction* (Addison-Wesley, Reading, MA, 1978), p. 286.

[24] E. E. Fullerton, I. K. Schuller, H. Vanderstraeten, and Y. Bruynseraede, Phys. Rev. B **45**, 9292 (1992).

[25] E. Bauer and J. H. van der Merwe, Phys. Rev. B **33**, 3657 (1986).

[26] J. H. van der Merwe, Surf. Sci. **449**, 151 (2000).

[27] J. H. van der Merwe and D. L. Tonsing, Surf. Sci. **449**, 167 (2000).

[28] I. Hernandez-Calderon and H. Hochst, Phys. Rev. B **27**, 4961 (1983).

[29] H. J. Elmers and U. Gradmann, Surf. Sci. **304**, 201 (1994).

[30] M. Prutton, *Introduction to Surface Physics* (Clarendon, Oxford, 1994), p. 63.

[31] G. E. Crook, L. Daweritz, and K. Ploog, Phys. Rev. B **42**, 5126 (1990).

[32] Y. Henry, C. Meny, A. Dinia, and P. Panissod, Phys. Rev. B **47**, 15 037 (1993).

[33] A. Cole, B. J. Hickey, T. P. A. Hase, J. D. R. Buchanan, and B. K. Tanner, J. Phys.: Condens. Matter **16**, 1197 (2004).

[34] J. P. McTague and A. D. Navaco, Phys. Rev. B **19**, 5299 (1979).